# Numerical investigation of a segmental grey cast iron tunnel ring: validation with laboratory data and application to field conditions

Agustin Ruiz López*, Aikaterini Tsiampousi*, Jamie R. Standing* and David M. Potts*

*Department of Civil and Environmental Engineering, Imperial College London, United Kingdom

September 2021

*Accepted version of the paper submitted to Computers and Geotechnics*

Corresponding author at: Imperial College London, Dpt. of Civil & Environmental Enginnering, Skempton Building, London SW7 2AZ, UK.
E-mail address: aikaterini.tsiampousi@imperial.ac.uk (A. Tsiampousi).

**ABSTRACT**

The structural response of a segmental grey cast iron (GCI) tunnel lining ring under distortion was investigated by means of finite element (FE) analysis. Building on previous experimental investigations, a 3D numerical model, capable of reproducing accurately the behaviour observed in the laboratory, was developed with the aim of providing guidelines for the structural assessment of GCI linings in engineering practice. A comprehensive validation of the segmental ring model with the laboratory data was first completed. Subsequently, a parametric study was conducted using a set-up that replicated the widely adopted elastic continuum method, so that differences between the numerical and the analytical solution could be attributed to the presence of the longitudinal joints. In this manner, the influence of the joints on the ring response was quantitatively established and recommendations for routine engineering calculations developed. A set of bending stiffness reduction factors are proposed as a function of the tunnel ovalisation, providing upper and lower limits of the bending stiffness, as well as a global reduction factor which is an average measure of the bending stiffness reduction. These factors can be integrated into the calculation procedure of closed-form solutions in order to account for the segmental nature of GCI linings.

Keywords: grey cast iron, segmental lining, tunnel joints, bending stiffness reduction factor

## 1. Introduction

During the late 19$^{th}$ and early 20$^{th}$ centuries London underwent a major development of the underground railway with the construction of deep tunnels in the London Clay strata. In those early times of tunnel construction, from 1894 to 1937, bolted GCI linings were routinely specified for the deep tunnels in the London Underground (LU) network (Craig and Muir Wood, 1978). As a general description, a bolted GCI lining is built as a succession of rings, each ring formed by six (or more) larger segments and a smaller closing key. The segments and rings are bolted together at the longitudinal and circumferential joints, respectively. Since there are numerous tunnels of this kind across the LU space, these are routinely affected by newly constructed underground structures such as excavations, deep foundations and tunnels. When such interactions take place, an estimation of how the existing tunnel deforms and additional internal forces develop from the new construction works is required in order to establish whether their magnitudes remain within the limits prescribed by LU and to determine whether special protective measures are required. This assessment, however, requires knowledge of the existing tunnel lining stiffness in both circumferential and axial directions, which are difficult to determine due to the presence of the tunnel joints. There is also considerable uncertainty about current internal forces within the GCI tunnels and their response to further ground movements.

A major research project was undertaken between 2010 and 2014 at Imperial College London (Standing et al.), comprising laboratory testing of bolted GCI segments, field instrumentation and FE modelling, to gain a better understanding of the response of GCI tunnels during tunnelling works in their near vicinity. The experimental investigation involved testing half-scale GCI tunnel segments bolted together and cast with a similar chemical

composition as that in Victorian tunnel linings. Three sets of experiments were conducted: tests on two segments bolted together under zero hoop force (Tsiampousi et al., 2017); tests on a segmental ring imposing only elastic distortions (Yu et al., 2017); and, large distortion tests in which the segmental ring was taken to failure (Afshan et al., 2017). Thus, the response of a bolted GCI ring could be investigated in the laboratory providing invaluable information regarding the behaviour of the joints and their influence on the ring response. Among other findings, it was shown that a segmental GCI ring behaves similarly to a continuous ring for small ovalisations at high overburden pressures (24 m depth) while under a large ovalisation, it experiences significant stiffness reductions near the joint locations. The first part of the study presented here was to model the tests numerically.

The behaviour of GCI linings has also been investigated numerically by others. Li et al. (2015) conducted an extensive parametric study on the structural response of a segmental GCI ring surrounded by springs to model the soil reaction. The authors demonstrated that the segmental GCI ring was significantly more flexible than a continuous ring by comparing the numerical results with an analytical solution. However, they did not demonstrate that a similar numerical model of a continuous ring (i.e. without joints) could replicate the analytical solution, and therefore it is not clear whether the differences in the results are attributable solely to the influence of the joints. Moreover, the behaviour of the bolted joint was calibrated (Li et al., 2014) using results from two-segment laboratory tests conducted by Thomas (1977) with no hoop force and therefore not akin to the conditions modelled in their segmental ring investigation.

Analytical solutions (Morgan, 1961, Muir Wood, 1975, Duddeck and Erdmann, 1985) play a significant role in the structural analysis of tunnel linings because of their ability to produce estimates of internal forces and displacements without the complexities involved in more sophisticated methods, such as FE analysis. These solutions are usually formulated assuming a continuous lining structure in segmental linings, with a reduction factor $\eta$ applied to the bending stiffness (EI) to account for the influence of the joints. Muir Wood (1975) proposed an empirical reduction factor $\eta$ related to the number of joints per ring which is widely adopted in practice. However, the recent experimental evidence (Yu et al., 2017, Afshan et al., 2017) suggests that its applicability to GCI linings might be limited. Reduction factors $\eta$ have also been derived analytically (Lee and Ge, 2001, Blom, 2002), based on the results of parametric numerical studies (Teachavorasinskun and Chub-uppakarn, 2010) and from laboratory model tests (Ye et al., 2014), however, the specific geometry and behaviour of bolted GCI joints are yet to be considered and therefore, the development of reduction factors for segmental GCI tunnel linings remains an open question.

This paper presents a number of 3D FE analyses carried out to model a segmental GCI ring with the Imperial College FE program ICFEP (Potts and Zdravkovic, 1999). The calibration and validation of the numerical model is first introduced with a series of analyses aiming to replicate the laboratory tests performed at Imperial College on the half-scale GCI segmental ring. Thus, a comprehensive validation process was achieved providing confidence in the capabilities of the numerical model to make engineering predictions. Subsequently, a series of

analyses was conducted with boundary conditions replicating those in the elastic continuum method of Duddeck and Erdmann (1985). A parametric study was then performed to evaluate quantitatively the influence of the joints on the structural response of a prototype LU tunnel at varying degrees of tunnel ovalisation. By comparing the segmental ring response with that of a comparable continuous ring, a set of reduction factors $\eta$ that accounts for the influence of the joints in commonly adopted analytical solutions is proposed.

## 2. Description of the experimental set-up

The experimental set-up and testing programme have been described in detail by Yu et al. (2017) and Afshan et al. (2017). A summary focusing on the aspects governing the boundary conditions used in the numerical analysis is provided here for clarity.

The testing was performed on a single half-scale ring (internal diameter of 1781 mm and width of 254 mm) that was formed by six equally sized segments, omitting the key segment for simplicity, connected with three bolts at each of the longitudinal joints. Ball bearing roller pads minimised friction between the ring and the floor where it rested horizontally. The load was applied radially by computer-controlled actuators acting on spreader pads with a 5° spacing between them transmitting the load to the ring extrados, to achieve a uniformly distributed load (Figure 1). The 0º angle ($\theta$) is set at the nominal crown of the ring and increases clockwise, such that joints are located at 0º, 60º, 120º, 180º, 240º and 300º. To prevent rigid-body movement, the actuators at 250º and 290º were replaced by reaction rods and ring rotation was restrained at 90º by a rod acting tangentially to it. Loading involved two stages: a confinement stage, where equal normal loads were applied via the actuators to generate hoop force; and a distortion stage, where the displacement of the actuator at axis level (90º) was controlled to achieve the desired radial distortion. During the latter stage, the load on all other actuators was maintained, with the exception of the one between the two reaction rods (270º), where the average load measured by load cells on the two rods was applied.

Regarding instrumentation, the force applied by each actuator was recorded with load cells and radial displacement at corresponding positions on the intrados of the lining by displacement transducers. Joint opening was measured at four joints using LVDT transducers attached to both the intrados and extrados of the ring at three locations along the longitudinal flange width (at the outer edge of the flange and aligned with the outer and middle bolts); forces in the bolts were measured using strain gauges; and axial forces and bending moments within the segments were estimated from strain gauge measurements at selected cross-sections around the ring.


*Figure 1 Schematic drawing of the laboratory setup (modified from Yu et al., 2017)*

In the small distortion tests reported by Yu et al. (2017) the influence of tunnel depth and bolt preload under essentially elastic conditions was investigated by applying actuator loads of 10 kN, 20 kN and 40 kN (equivalent to overburden pressures at 6, 12 and 24 metres, respectively, assuming isotropic stresses) and preloading the bolts to 5, 7.5 and 10 kN, in series of parametric studies. Tests for each load combination were performed three times to assess the repeatability of control and measurements. The bending moments for 40 kN confinement load compared well with the analytical solution of a continuous ring (Young and Budynas, 2002), which in conjunction with the observation that negligible joint opening occurred, suggests that, despite its segmental nature, the ring behaviour approached that of a continuous ring for the highest confinement load. The experimental results revealed that joint opening increased as the confinement reduced, diverging from the analytical solution of a continuous ring. Furthermore, it was shown that with a compressive hoop force acting on the joints, the magnitude of the bolt preload was not significant with little differences in the ring response for the different values considered. Based on these observations, the case for 40 kN confinement load and 5 kN bolt preload was simulated as a calibration exercise, as explained later, while the remaining tests by Yu et al. (2017) were used to validate the numerical model.

Afshan et al. (2017) report on additional tests performed to assess the ultimate capacity of the ring, under 40 kN confinement load. The distortion stage was continued until failure was reached, in either the segment or the joint. During the first attempt (Test 1), a diametric distortion of 42.1 mm (2.36% diametric distortion) was reached without signs of failure. This was more than double the magnitude (18.7 mm) at which the authors predicted the ring would fail at two symmetrical joint locations. After a fifteen-hour shift, the test had to stop for health and safety reasons and the ring was unloaded completely. Before repeating the test (Test 2), the

bolts at the most compromised joint locations were replaced by new ones to ensure that potential yielding during Test 1 would not cause premature failure of the joints. In Test 2, the ring fractured at a diametric distortion of 35.3 mm (1.98% diametric distortion), in both circumferential flanges of the segment on one side of the joint at $\theta$=180$^o$, very close to the intersection of the circumferential and the longitudinal flanges, propagating from the intrados towards the skin. Only Test 1 was used in the validation of the numerical model, because of uncertainties about the effect of the unloading-reloading cycle in Test 2.

## 3. Description of the numerical model

### 3.1 Geometry and finite element mesh

The 3D finite element mesh employed in the analyses is shown in Figure 2a. Due to symmetry around the axis of the ring, only the top half was modelled. The geometry of the segments, in particular the connections at the joints, was reproduced in detail, including the caulking groove, the bolting system comprising the bolt, nut and washer and the corresponding bolt holes. The geometry and dimensions of the joint are included in Figure 2b. The contact between the segments at the longitudinal joints was modelled with zero thickness interface elements (Day and Potts, 1994). Tsiampousi et al. (2017) demonstrated the need to calibrate their stiffness carefully, as it has considerable impact on the analysis results. For this reason, rather than including interface elements between the different components of the bolting system and between the washers and the longitudinal flanges, physical compatibility was assumed. High-order 20-noded solid elements were employed for the segments and bolting system and 16-noded interface elements for the contact between segments.

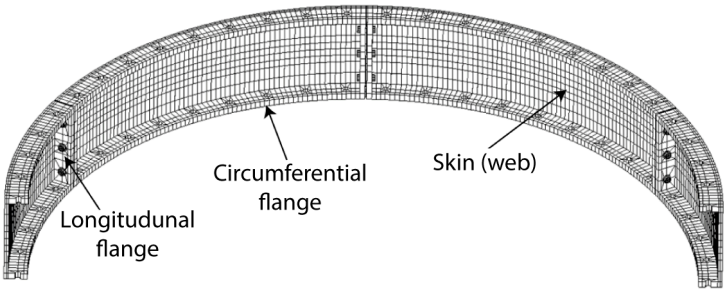


(a) Finite element mesh

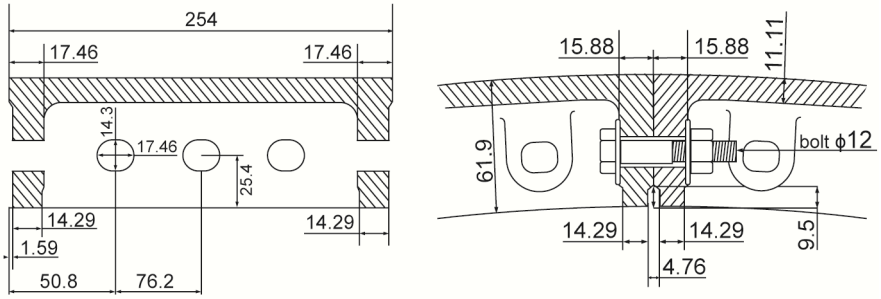


(b) Longitudinal joint (dimensions in mm)

*Figure 2 Geometry of the finite element model*

## 3.2 Boundary conditions

Due to symmetry, the nodes on the cross-sections at 90º and 270º were fixed in the normal direction (Figure 3). The nodes along the contact area where the circumferential flanges rested on the floor were also fixed in the normal direction. It was assumed that, for the test conditions, the self-weight could be neglected in the analysis.

Each analysis was performed over three stages comprising bolt preload, confinement and distortion as in the experiment. To simulate the bolt preload, the nuts on one side of each joint were removed from the mesh prior to the start of the analysis. A tensile load representative of the bolt preload was then applied on the exposed surface of the threads, with an equal and opposite load applied on the exposed surface of the corresponding washers. Subsequently, the nuts were activated, completing the bolt preload sequence. In the confinement stage, a radial stress $p_{act}$ was applied to the extrados of the ring over surface areas (each 250x250 mm) corresponding to those of the plates employed in the laboratory to transfer the load from the actuators (see Figure 3a). Two different boundary conditions, applied over the same surface area as for the actuator loads, were investigated to model the presence of the two reaction rods: a radial fixity, assuming an infinitely stiff reaction bar; and a radial spring, representing a finite stiffness of the reaction system. This process formed part of the calibration of the numerical model and is discussed in a subsequent section.

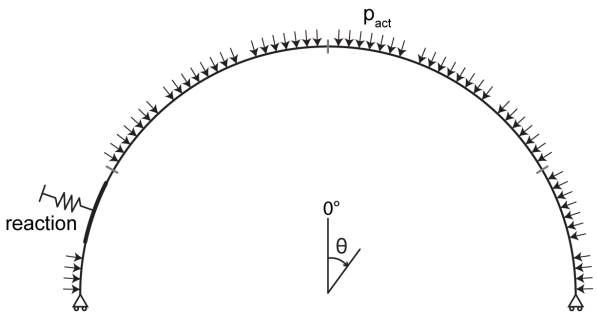


(a) Confinement stage

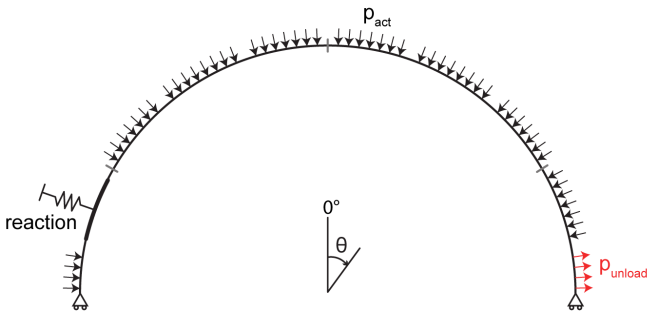


(b) Distortion stage

*Figure 3 Schematic plan view of boundary conditions and loading*

The distortion of the ring was applied by reducing the load on the axis level (90º) actuator, see Figure 3b, in small increments until the target distortion was reached within reason, while maintaining the confinement stage load at all other locations, including the actuator at 270º where the load in the test was adjusted according to the measured load changes in the reaction rods. This simplification means that all the load changes in the analysis were taken by the two segmental areas relating to the reaction rods rather than being distributed over a larger area of the segment as in the experiment.

## 3.3 Material properties

### 3.3.1 GCI segments

A number of elastoplastic models (Hjelm, 1994, Altenbach et al., 2001, ABAQUS, 2014) have been proposed in the literature to reproduce the observed mechanical response of GCI: uniaxial strength in compression is typically 3-4 times higher than in tension (Angus, 1976); the stress-strain relationship in tension is nonlinear and permanent strains are generated from early stages of loading; significant permanent volume increases occur under tensile stress states (Gilbert, 1972, Coffin, 1950).

For reasons of convenience, the constitutive model implemented in ICFEP by Schutz (2010) was adopted and modified to reproduce the behaviour of GCI. Originally developed for the modelling of shotcrete, it is formulated as a multi-surface, associated plasticity model. In tension, the yield surface is derived from the Rankine failure criterion, while in compression the option of employing the von Mises failure criterion, which is appropriate for GCI, is available. The two surfaces are allowed to evolve independently, with the principal plastic strains $\varepsilon_1^p$ and $\varepsilon_3^p$ being the hardening variables for the tension and compression surfaces, respectively.

The modification of the model relates to the pre-peak hardening behaviour, which was adjusted to capture adequately the nonlinearity of the experimental GCI stress-strain curve, as summarised in Appendix A1. The modified model was validated using results from tests performed by Coffin (1950) under a range of loading paths, demonstrating very good overall correspondence with the experimental data (Appendix A2) .

In Figure 4 the stress-strain response from the constitutive model in a single element simulation of uniaxial tensile loading is compared with those from coupon tests conducted by Yu (2014) on the same GCI used for casting in the ring segments. The new hardening law reproduced well the stress-strain curves measured in the laboratory. A Young's modulus *E* of 100 GPa and a Poisson's ratio $\nu$ of 0.26 were adopted, while the remaining model parameters are presented in Table A1 (Appendix A3). As no data are available for the compressive behaviour of this GCI, it was assumed that yield and peak strength in compression are four times larger than those in tension (Angus, 1976). Strain-softening was not considered, even though the constitutive model could account for it (see Appendix A1), since the analyses presented in this paper were not intended to model fracturing of the GCI.

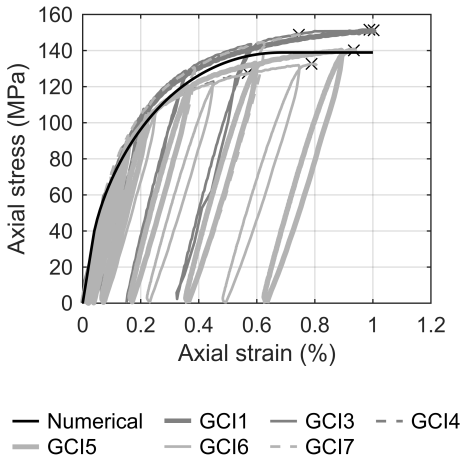


*Figure 4 – Uniaxial tensile test simulation compared with the results from coupon tests conducted by Yu (2014) – black crosses mark test failure points*

3.3.2 Interface elements

Interface elements (Day & Potts, 1994) were employed to model the segment to segment contact at the joints. The elastic perfectly-plastic Mohr-Coulomb model was adopted with an angle of shearing resistance of 40º, as in Tsiampousi et al. (2017). While in compression, the joint elements were elastic and their behaviour governed by their normal and shear stiffness. When in tension, the interface elements were open and their stiffness was zero. Using appropriate stiffness values is crucial for obtaining accurate results in contact problems. Ideally, they should be high enough to minimise penetration between contacting bodies, but values that are too high may result in numerical instabilities.

Tsiampousi et al. (2017) established through calibration an interface stiffness value of $10^7$ kN/m$^3$ for the two-segment test under zero hoop force. However, as a hoop force was imposed in the full ring tests simulated here this value was not necessarily appropriate and so further calibrations to obtain the interface stiffness were performed as discussed in Section 4.2.

3.3.3 Mild steel bolts

The mechanical behaviour of the bolting system was modelled with the elastic perfectly-plastic von Mises model. The Grade 4.6 mild steel bolts employed in the experiments have a yield strength of 240 MPa, which is the only plastic parameter required by the model.

Although the elastic modulus of Grade 4.6 mild steel is 210 GPa, Tsiampousi et al. (2017) concluded that the stiffness of the bolting system should be reduced to 50 GPa in the numerical analysis to account for compliance, when the bolts are modelled as a single component, ignoring the interfaces between the individual components. Hence, the elastic modulus of the bolting system was set to 50 GPa.

## 4. Calibration of the numerical model

When translating the experimental set-up into a numerical model there was uncertainty regarding the boundary condition that should be used to simulate the presence of the reaction

rods that replaced actuators at 250º and 290º. In phase one of the calibration different approaches are explored to decide on the most effective boundary condition. Furthermore, the stiffness of the interface elements at joints needed to be calibrated. This is done in phase two.

The small distortion test by Yu et al. (2017) at 40 kN confinement load and 5 kN bolt preload was selected to calibrate the numerical model. The fact that a stiffness similar to that of a continuous ring was established in the test (due to negligible joint openings) allowed the use in phase one of a continuous ring model, similar to that in Figure 2 but without interface elements. Having eliminated the need to quantify the interface element stiffness, focus was placed on selecting an appropriate boundary condition for the reaction rods. In phase two, the selected boundary condition was applied to the segmental ring model (i.e. with interface elements), progressively increasing the interface stiffness in successive analyses, until the analysis results matched the continuous ring and the experimental results.

## 4.1 Phase one: Reaction rod boundary condition

Three different boundary conditions were considered at the reaction rod locations along the extrados: 1) radial fixity; 2) radial spring (i.e. normal to the surface) with a stiffness representative of the dimensions and material of the bar in the laboratory; and 3) radial spring with a stiffness reduced to 1/10 of the stiffness employed in 2). The latter condition was to account for the potential compliance of the system connecting the bar to the external reaction ring.

The results from the three simulations were compared with the laboratory data in terms of the change in radius at nine locations around the ring (Figure 5a) and the change in bending moment during the distortion stage (Figure 5b), note that the numerical results from 90º to 180º were obtained by symmetry. To be consistent with Yu et al. (2017), the radius change was taken as the change in diameter divided by two, such that the results are a measure of the distortion all around the ring. It can be observed that all three analyses reproduced adequately the distortion around the ring, with the case of reduced spring stiffness giving the best comparison with the laboratory data at 10º (170º) and 50º (130º), where the analyses slightly overestimate the change in radius. The same analysis provided the best match to the experimental data of change in bending moment around the ring. As expected, the bending moment became progressively larger as the rigidity of the boundary condition increased. Furthermore, the boundary condition affected the shape of the bending moment distribution, particularly near 0º, 90º and 180º. Based on these observations, it was concluded that the radial spring with reduced stiffness was the most appropriate condition and was adopted in all subsequent analyses (the other two cases provided an excessively rigid restraint).

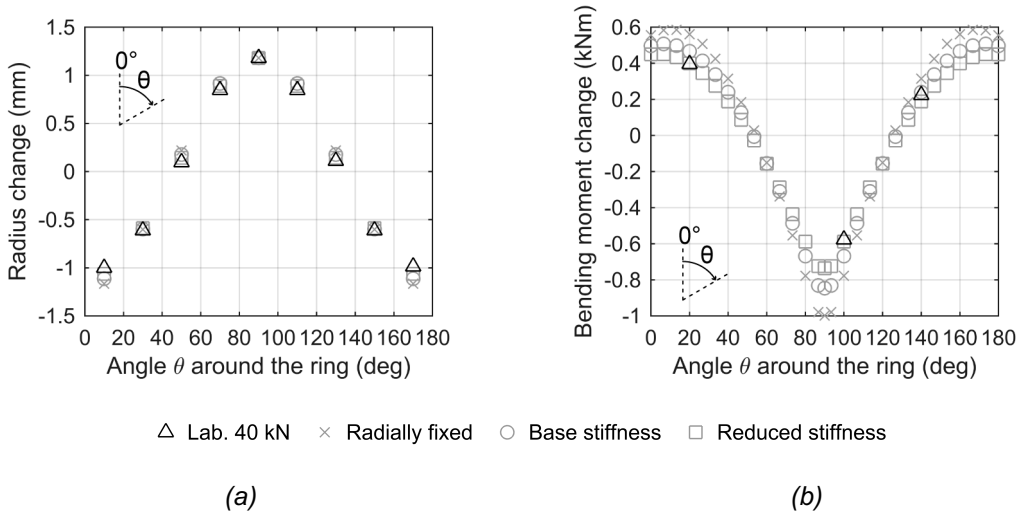


*Figure 5 Evaluation of reaction rod boundary condition (a) radius change (mm) (positive outwards) and (b) bending moment change (kNm) (M+ tension intrados)*

## 4.2 Phase two: Interface element stiffness

The normal and shear stiffness of the interface elements in the segmental ring model were changed parametrically considering values of $10^8$ kN/m$^3$, $10^9$ kN/m$^3$ and $10^{10}$ kN/m$^3$. The unloading force (at $\theta$=90º) required to achieve the target distortion in phase one was applied in all the simulations. Figure 6 compares the change in radius obtained from the three analyses and for a continuous ring. It can be observed that with increasing interface element stiffness the distortion around the ring converges towards that of the continuous ring, with the analysis using $10^{10}$ kN/m$^3$ reproducing accurately the continuous ring model. Hence, the normal and shear stiffness of the interface elements was set to$10^{10}$ kN/m$^3$ in all subsequent analyses, a much stiffer value being required than that established by Tsiampousi et al. (2017).

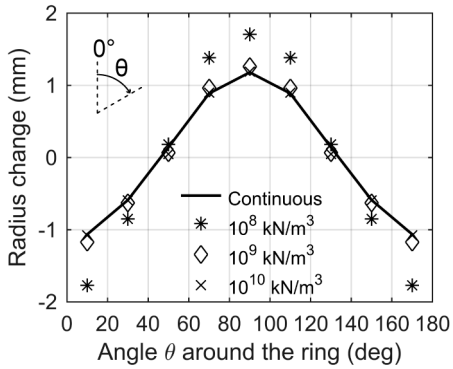


*Figure 6 Radius change (mm) around the ring for varying interface element stiffness (positive outwards)*

## 5. Validation of the numerical model

Once the model parameters controlling the rigidity of the segmental GCI ring were calibrated, the ability of the numerical model to reproduce the joint opening and stiffness reduction observed in the experimental ring was assessed. The validation considered distortion magnitudes under (elastic) serviceability and (near) ultimate state conditions and therefore, included a series of analyses simulating the parametric study conducted by Yu et al. (2017) and the large distortion test (Test 1) carried out by Afshan et al. (2017).

### 5.1 Small distortion tests

In the small distortion tests by Yu et al. (2017) the magnitude of the bolt preload had a negligible impact in the ring response, and therefore, in the validation of the numerical model only the set of tests with bolt preload of 5 kN was considered. Actuator loads of 10 and 20 kN, equivalent to overburden pressures at 6 and 12 m, respectively, were considered in addition to the 40 kN (24 m overburden) which was used in the calibration.

The predicted changes in radius for the three confinement loads are presented in Figure 7a. Due to the negligible differences in the laboratory data of the three tests, only one set of measurements representative of all the tests is included in Figure 7a for clarity. The numerical results were evaluated at the analysis increment where the computed distortion matched the experimental at 90º. Negligible differences between the three numerical analyses and good agreement with the experimental data are observed.

Figure 7b depicts the change in bending moment around the ring corresponding to the distortion level presented in Figure 7a. The experimental bending moments were determined from the strain gauge measurements at 20º, 100º and 140º for the three laboratory tests (note that only the results from one of the three repeated tests performed is included). The experimental results show a reduction in the ring stiffness with decreasing confinement load. The numerical results indicate a smaller variation of bending moment with confinement load than that observed experimentally, with the results obtained for 20 and 40 kN confinement load being identical and comparable to the laboratory data for 40 kN. Although the change in bending moment for the analysis with 10 kN confinement load showed a slight reduction around 0º and 180º with respect to the other two analyses, this was less than the reduction observed in the laboratory. Consequently, the segmental ring model did not capture the entire extent to which the ring stiffness reduced with reducing confinement loads in the laboratory.

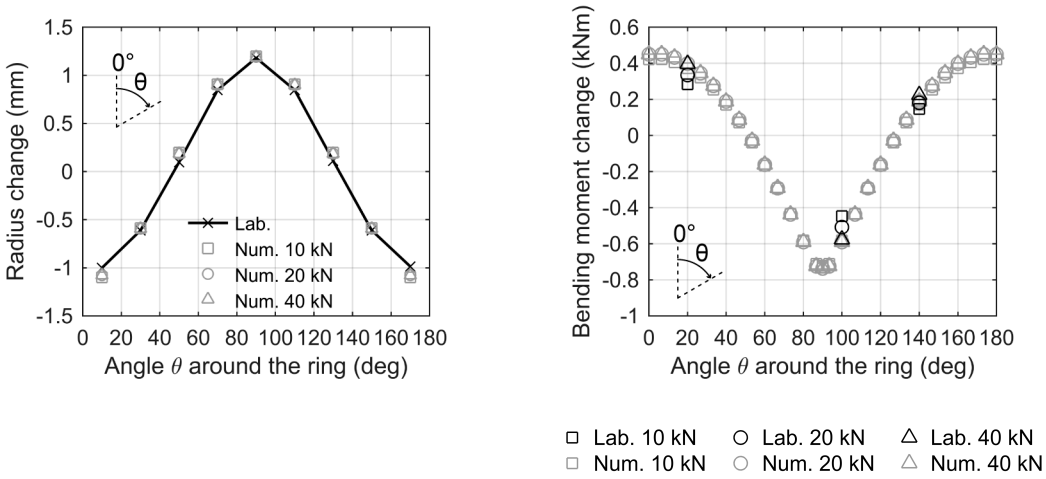


*(a)* *(b)*

*Figure 7 Small distortion test at confinement loads of 10 kN, 20 kN and 40 kN (a) radius change (mm) (positive outwards) and (b) bending moment change distribution (M+ tension intrados)*

The circumferential displacement at the intrados of the upper edge of the joints on the right half of the ring (0º-180º) for the three confinement loads is presented in Figure 8a. Positive displacement signifies opening of the joint. The laboratory measurements of the repeated tests are all included in the figure. Although repeatability is not as good as in the case of change in bending moment, larger circumferential displacements (opening of the joints at 0º and 180º and closing at 60º and 120º) for smaller confining loads were consistently measured in the experiments. The influence of the confinement load on the joint opening is also evident in the analysis, however, for 20 and 40 kN confinement load, in addition to the joints at 60º and 120º, the joints at 0º and 180º remained closed, explaining the similarity in the computed bending moments between the two analyses. On the contrary, the joints at 0º and 180º for the analysis with 10 kN confinement load opened, justifying the stiffness reduction observed in Figure 7b compared with the other two analyses.

The opening of the joint at 0º (positive bending moment) for 10 kN confinement load is further investigated in Figure 8b, which depicts the displacement along the intrados at the three locations indicated in the figure: aligned with the middle bolt centreline (0 mm), with the edge bolt centreline (76 mm) and with the edge of the joint (127 mm). The model response shows a qualitative agreement with the laboratory data, with maximum opening at the edge of the joint and negligible movement at the middle bolt location. This behaviour is associated with the geometry of the segment cross-section, as the stress transfer along the height of the longitudinal flange is influenced by the presence of the circumferential flanges at the joint edge and the tension causing joint opening originates from there.

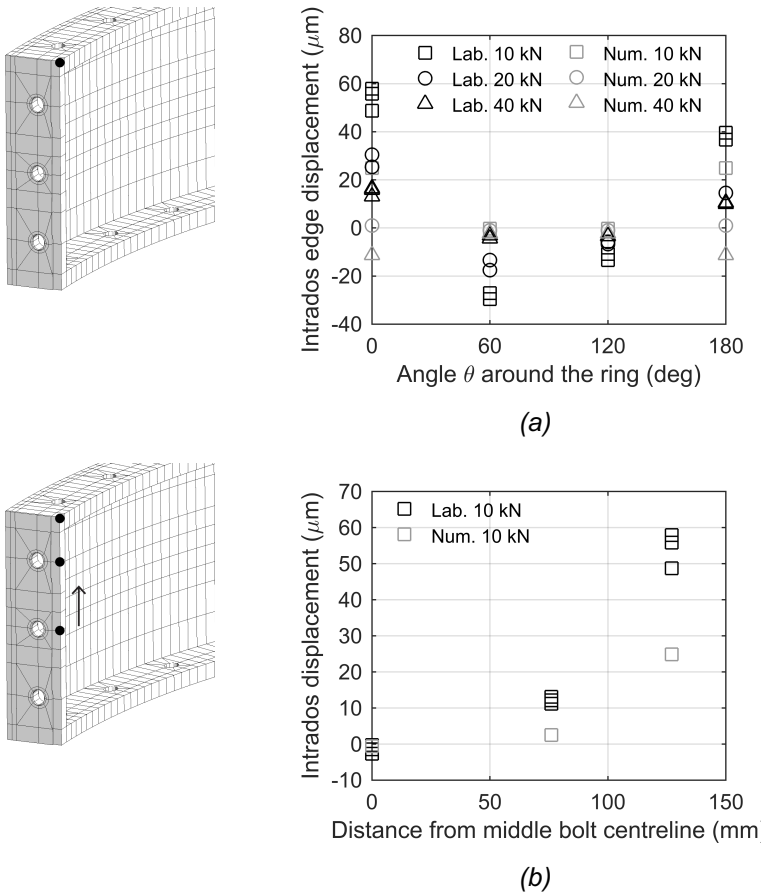


*Figure 8 Displacement (μm) at the intrados (a) at the upper edge location of joints around the ring for all confinement cases (b) along the intrados of the 0º joint in the 10 kN load case (opening is positive)*

It can be concluded that the numerical model captures the reduction in the ring stiffness with joint opening as observed in the laboratory. The underestimation of the joint movements at small distortions and, as a consequence, the overestimation of the ring stiffness when joint opening occurred, could be attributed to imperfections in stress transfer across the joint, which were not included in the numerical model, where joint plates were perfectly flat and segments perfectly aligned. This is further explored in Appendix B, where a small perturbation of 5% in the applied confinement load applied by some of the actuators is shown to produce numerical results in excellent agreement with the laboratory data.

## 5.2 Large distortion test

The validation exercise was extended to the large distortion Test 1 by Afshan et al. (2017). Following bolt preloading to 7.5 kN and radial confinement of 40 kN, unloading in the numerical analysis was performed incrementally until the radial displacement at 90º matched the laboratory data (42.1 mm).

Figure 9a presents the change of radius all around the ring, exaggerated ten times for illustration purposes. Due to symmetry, the numerical results were mirrored around the ring axis. Overall, excellent agreement is found between the numerical and laboratory results; the

distorted shape illustrates the influence of the reaction bars at 250º and 270º, highlighting the importance of having selected an appropriate boundary condition from the calibration.

The computed change in bending moment during the distortion stage is compared with the laboratory data in Figure 9b. Despite under-predicting the bending moment at 90º, the shape of the numerical curve is reasonable and in excellent agreement with the experimental results at all other locations (20º, 40º, 100º, 140º and 160º). Yu (2014) discussed the potential for relative errors up to 15% in bending moments obtained from strain gauge measurements, which could partly explain the discrepancy with the laboratory data at 90º.

Figure 10a presents the opening of the joint at 0º/180º (where the maximum movements were recorded) with the increase in displacement at 90º during the distortion stage of the test at three locations at the intrados: at the upper outer edge of the longitudinal flange and aligned with the top and middle bolt centrelines (similar to the sketch in Figure 8b). The numerical results compare remarkably well with the laboratory data, capturing accurately the gradual change in joint opening from the outer edge (about 2 mm) towards the middle bolt (approximately 0.2 mm), which was also observed for small distortions albeit with much smaller magnitudes (Figure 8b). The behaviour of the 0º joint is further examined in Figure 10b where the change in bolt load for the outer and middle bolts during distortion at 90º is presented. Consistent with the observations made for joint opening, the change in bolt force is significantly larger for the outer than for the middle bolt. The numerical results for the outer bolt match very well with the experimental measurements up to a displacement of about 30 mm, where the bolt in the numerical analysis yielded and reached a plateau (as perfect plasticity was adopted). The corresponding experimental curve gives no evidence of yield, potentially because it was derived from strain gauge measurements considering linear behaviour (Afshan et al. (2017). This reveals a failure mode of the joint, not realized during the experimental investigation, where the outer bolts yield in tension prior to the GCI reaching its ultimate tensile strength at the circumferential flange near the joint. Regarding the middle bolt, the predicted increase in force again agrees well with the experimental data up to a displacement of 30 mm, but increases rapidly subsequently, as the outer bolts yield and additional tensile loads are transferred to the middle bolt, diverging from the experimental data which show a gentler increase and transfer of loads.

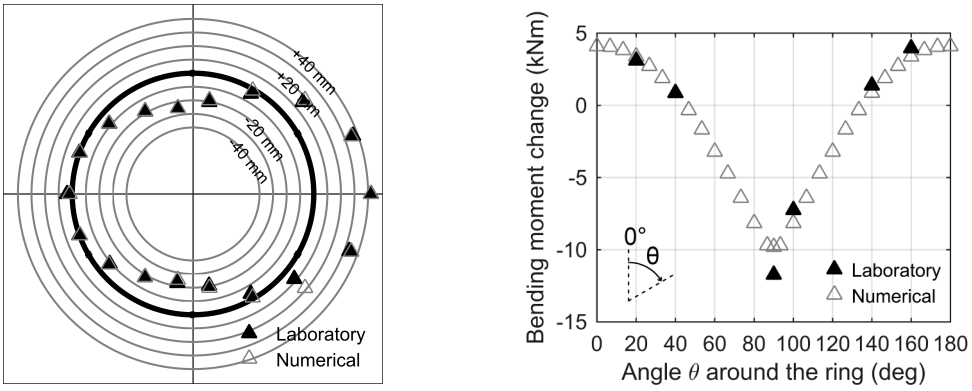


*(a)* *(b)*

*Figure 9 (a) Radius change (mm) and (b) bending moment change (kNm)* (M+ tension intrados) *around the ring at the end of Test 1*

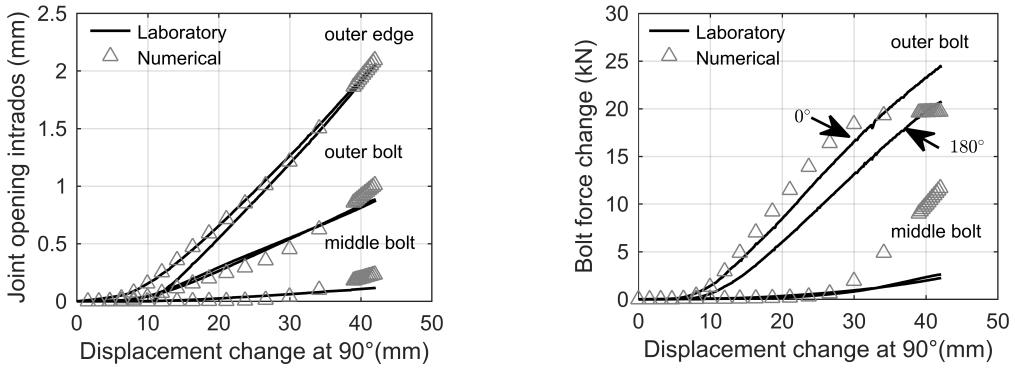


*(a)* *(b)*

*Figure 10 Evolution at 0º/180º of (a) opening (mm) along the intrados and (b) bolt force (kN) change during the distortion stage*

The evolution of plasticity in the ring with increasing distortion was studied in the numerical analysis. Contours of the deviatoric plastic strain $\mathrm{E}_{\mathrm{d}}^{\mathrm{p}}$ at four distortion levels are presented in Figure 11. Plastic strains first appear due to tension at the intrados near 0º and at the extrados near 90º. With further distortion, the plastic zone gradually propagates, including yielding in compression at the intrados at 90º and in compression and extension at the intrados and extrados respectively from 270º to 300º. By the end of the test (Figure 11d), the maximum plastic strains are concentrated around the 0º joint, at the connection between the longitudinal and circumferential flanges. This is where the segment fractured in Test 2 (in the symmetric segment at 180º).

Maximum principal strains $\varepsilon_1$ at this section are shown in Figure 12, with the upper plots focusing on the intrados of the segments in the vicinity of the joint and the lower plots on the face of the longitudinal flange in contact with the neighbouring segment. Significant tensile strains develop along the intrados of the circumferential flanges, propagating along the edges of the joint, at the intersection between the longitudinal and circumferential flanges, and the intrados of the skin where it joins with the longitudinal flanges. The maximum tensile strains $\varepsilon_1$ (0.45% and 0.42%) occur at the intrados of the circumferential flange, in the numerical

integration points closest to the longitudinal flange and were slightly smaller than the lowest axial strain (0.57%) at which any of the GCI coupons tested by Yu (2014) failed (see black crosses in Figure 4), consistent with Test 1 where failure did not occur. The views of the longitudinal flange in the lower plots of Figure 12 reveal that plasticity was initially generated by the action of the outer bolts and only later by the middle bolt, towards the end of the test (Figure 12c). This can be correlated with the evolution of bolt forces in Figure 10b and the yielding of the outer bolts.

The results from the model validation are very encouraging as the model captures well the stiffness reduction experienced by the experimental ring at small (see also Appendix B) and large distortion levels. The stiffness reduction is adequately captured because of the good correspondence with the laboratory data in terms of joint opening and bolt forces as well as the ability of the constitutive model to reproduce the material response. The validation exercise provided confidence in the model's predictive capabilities and so an additional investigation was conducted aiming to quantify the influence of the joints within the context of the elastic continuum model, as is presented in the next section.

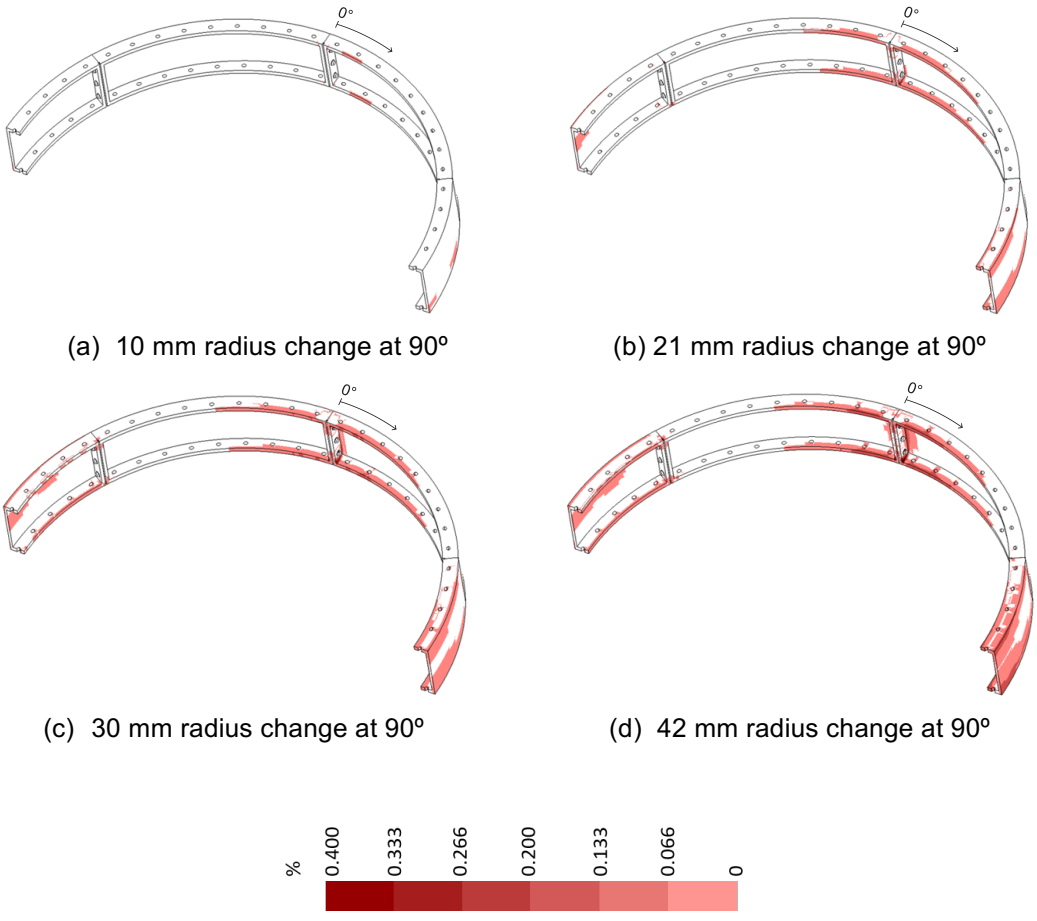


(a) 10 mm radius change at 90º

(b) 21 mm radius change at 90º

(c) 30 mm radius change at 90º

(d) 42 mm radius change at 90º

*Figure 11 Predicted deviatoric plastic strain $E_d^p$ (%) at various distortion levels during Test 1*

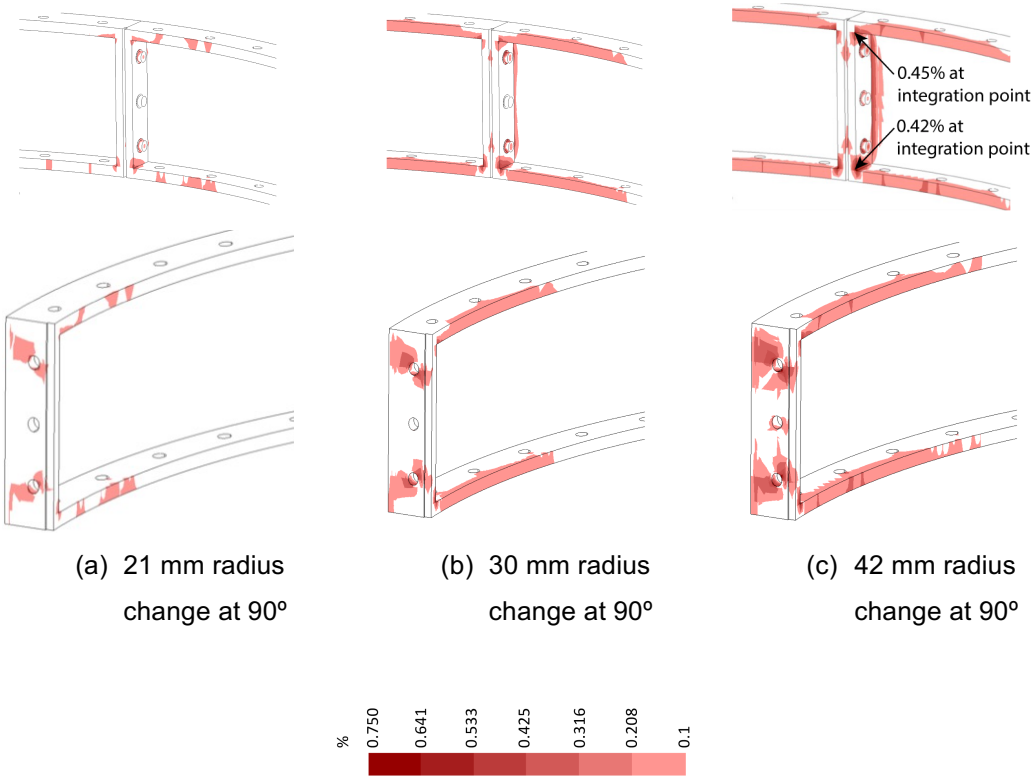


*Figure 12 Predicted maximum principal strain $\varepsilon_1$ (%) around the 0º joint at various distortion levels during Test 1*

## 6. Bending stiffness reduction due to longitudinal joints

As pointed out in the introduction, recent experimental evidence (Yu et al., 2017, Afshan et al., 2017) shows that the influence of the joints on the stiffness of a GCI tunnel ring crucially depends on the degree of ovalisation that it has experienced. Field measurements indicate that many of these tunnels develop significant squatting (i.e. enlargement of the horizontal diameter) over time, with horizontal diametric distortions ranging between 0.5 and 1% (Wright, 2013). Clearly, the stiffness reduction of GCI linings should be investigated at the ovalisation range usually observed in the field. The study presented here examined the influence of the joints at a range of squatting levels, comparing the structural response of the segmental GCI ring with that of a continuous ring in order to determine the appropriate reduction factor $\eta$ for a given tunnel ovalisation. The analyses were conducted within the framework of the elastic continuum method (Duddeck and Erdmann, 1985) which is widely adopted for assessing the internal forces within GCI linings.

## 6.1 Model set-up

The geometry of the model followed that of the half-scale experimental ring, in this case the model took advantage of symmetry such that only half of the segments width and a quarter of the ring circumference (from crown to axis level) were considered. The dimensions were doubled to replicate the size of a prototype tunnel (in particular the Central Line running tunnels beneath Hyde Park) with an internal diameter of 3.56 m. This tunnel geometry corresponds to a standard GCI running tunnel of the LU network (TfL, 2020). The ring was formed of six segments bolted together with joints spaced at 60º, with one of them aligned at the crown. This is the typical configuration employed in tunnels constructed in the 19$^{th}$ century and early 20$^{th}$ century where the longitudinal joints align between rings allowing for the analysis of a single ring to investigate the response along the axis of the tunnel. Note that the small key segment located at the crown was not considered allowing for symmetry conditions around the axis level to be applied.

Regarding the boundary conditions, at the axes of symmetry (i.e. crown, axis level and circumferentially along the middle of the segment) the displacements were restricted in the normal direction to the boundary. Furthermore, the outer boundary of the circumferential flange was fixed in the direction of the tunnel axis (i.e. perpendicular to the circumferential flange), this is then consistent with the continuum method, which considers a plane-strain condition. The soil loading can be divided into primary loading from the soil active pressures, and secondary loading from the ground reaction stresses. The primary loading was modelled by applying normal and shear stresses to the ring extrados. Only full bond conditions, where soil shear stresses are fully transmitted to the lining, were considered. A tunnel with its crown at 20 m depth was considered and, assuming that the full overburden acts on the lining, a total vertical stress $\sigma_v$ of 400 kPa and a total horizontal stress $\sigma_h$ of 280 kPa were applied, such that the ratio between $\sigma_h$ and $\sigma_v$ is adopted as 0.7 (as recommended by Tube Lines (2008)). A constant stress profile with depth along the tunnel height (see Figure 13) was adopted to enable a direct comparison with the analytical solution. The secondary loading was modelled with constant stiffness radial and tangential springs acting on the extrados. The stiffness of the radial and tangential springs, $K_r$ and $K_t$, respectively, was determined with the following expressions (Duddeck and Erdmann, 1985, Plizzari and Tiberti, 2006):

$$K_r = 0.6\frac{E_s}{R}$$

$$K_t = \frac{K_r}{3}$$

where $E_s$ is the constrained elastic modulus:

$$E_s = \frac{E_c \cdot (1-\nu)}{(1-2\nu)\cdot(1+\nu)}$$

where $E_c$ and $\nu$ are the elastic modulus and Poisson's ratio of the ground and R is the external radius of the tunnel. The stiffness of the springs was varied parametrically in order to assess the response at varying squatting magnitudes. The self-weight of the GCI ring was neglected to

comply with the assumptions of the analytical solution. A bolt preload determined from 25% of the bolt yield stress was applied in line with the laboratory findings described by Tsiampousi et al. (2017).The properties calibrated above for the GCI and the interface elements were adopted in the analyses. Although the elasto-plastic model for GCI described above was adopted for the longitudinal flanges, all other parts of the segments were modelled as linear elastic, such that differences with respect to the elastic continuum solution can be solely attributed to the influence of the joints. The bolts employed in the LU tunnels are often made of wrought iron with a characteristic ultimate tensile strength of 342 MPa (Tube Lines, 2008), the tensile yield stress for the elastic perfectly-plastic von Mises model was adopted as 239 MPa (70% of the ultimate strength as assumed by Yu (2014)). The calibrated value of 50 GPa for the elastic modulus of the bolting system was adopted (preliminary analyses revealed little sensitivity of the overall ring stiffness to the bolt stiffness value).

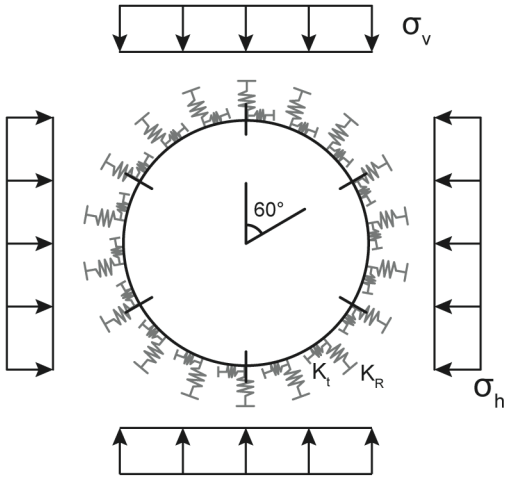


*Figure 13 Sketch of the FE model set-up*

## 6.2 Numerical results

Before making any comparisons between the results from the numerical analysis of the segmental ring and the analytical solution for the continuous ring, which would highlight the influence of the joints, the numerical model was checked to make sure that it could replicate the analytical solution. To this end, a numerical analysis using a continuous ring (i.e. without longitudinal flanges, but similar to the segmental ring in all other respects) was conducted, adopting ground properties of $E_c = 20$ MPa and $\upsilon = 0.2$. The numerical and analytical results are compared in Figure 14 in terms of (a) displacements, (b) bending moments and (c) axial forces. Note that the analytical results are only shown at the crown and axis level locations as the expressions given by Duddeck and Erdmann (1985) only considered the maximum values around the lining. There are only small discrepancies between the numerical and analytical solutions for the continuous model, and therefore any differences between the numerical

analysis of the segmental ring and the analytical solution of the continuous ring can be attributed to the presence of joints and not to inherent discrepancies between the numerical and analytical approaches.

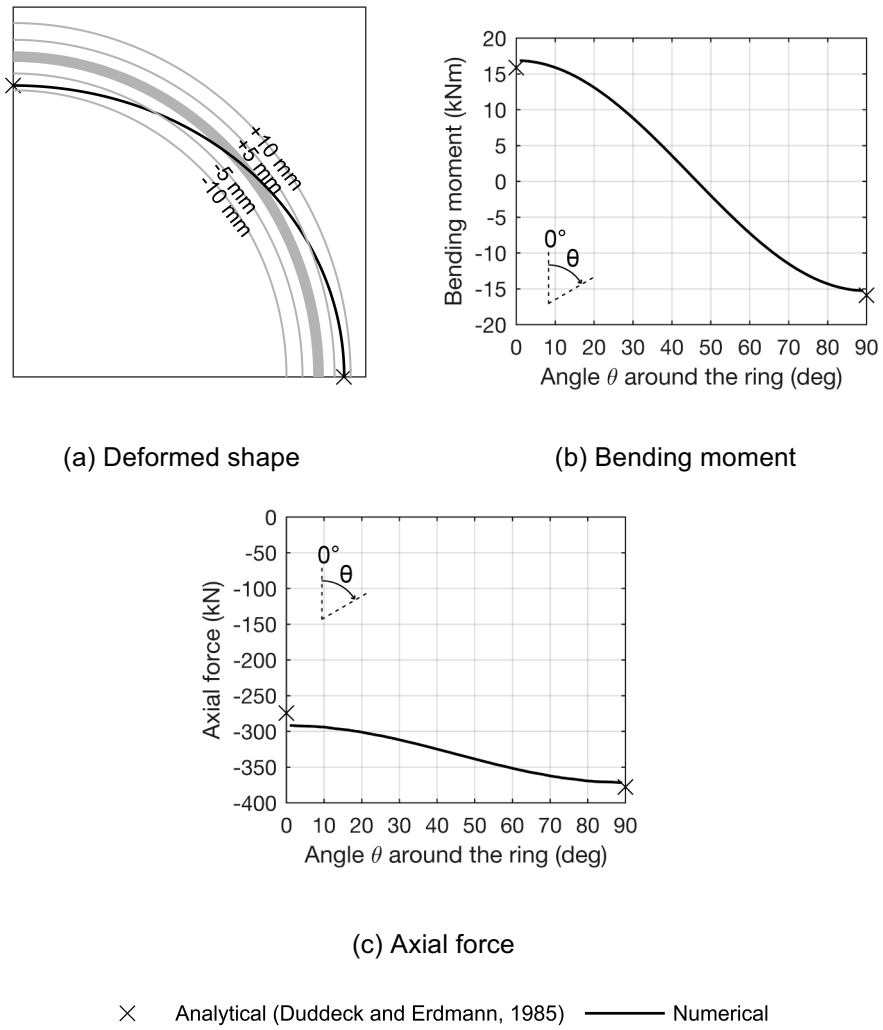


(a) Deformed shape

(b) Bending moment

(c) Axial force

*Figure 14 Validation of the continuous ring model ($E_c = 20$ MPa and $\upsilon = 0.2$)*

The bending moment distribution for the segmental and continuous ring models at approximately 1% squatting is depicted in Figure 15. Note that TfL (2017) recommends that 1% squatting be taken as the existing tunnel ovalisation when field data are not available. Starting with the continuous ring, the bending moment is highest at 0° and 90° (i.e. at the crown and the axis level), as expected. The ring experiences tension at the intrados at the crown and at the extrados at the axis level, as indicated by the bending moment signs in Figure 15. In comparison, the segmental ring experiences considerable stiffness reduction around the 0° joint, which opened by 0.68 mm at the intrados according to the analysis. Conversely, the stiffness at the 60° joint, which opened at the extrados but by a smaller degree (0.03 mm) than

the 0° joint, is very similar to that of the continuous ring. The difference in behaviour of the two joints is expected: the bending moment at which the joint opens is lower for the positive bending mode (tension at the intrados) as the section modulus is greater under this mode, and also the soil loading causes higher moments at the crown/invert (because of the ratio between $\sigma_h$ and $\sigma_v$). Consequently, under squatting, the 0° joint seems to be dominating the distribution of bending moments around the segmental ring, but its influence tends to diminish away from the joint. The bending moment at 90° is only slightly smaller than that of the continuous ring.

In order to assess the ring response under a range of ovalisations, the radial and tangential stiffnesses for the ground reaction were changed in a parametric study. In Figure 16 the bending moments at the crown and at the axis are plotted against the percentage of squatting for the segmental ring analyses along with the analytical solution adopting full bending stiffness ('rigid ring') and a reduced bending stiffness ('flexible ring') using Muir Wood's reduction formula. Note that data points plotted for each squatting magnitude correspond to individual FE simulations using different spring stiffness values. The squatting of the segmental ring cases varies between 0.23% and 1.81% which covers the range observed for the majority of LU tunnels (0.5-1%) and beyond. The stiffness reduction initially manifests itself more clearly at the crown for the reasons given when discussing the 1% squatting case (Figure 15). The segmental ring response is similar to that of the rigid ring for squatting levels below about 0.25% and becomes progressively softer for larger ovalisations. The bending moment at the axis level remains comparable to the rigid ring solution up to a squatting of approximately 0.7%, where it starts deviating from it more prominently because of the opening at the extrados of the 60° joint. The predicted segmental ring response is considerably stiffer than that of the flexible ring. Even at the crown (softest section) the bending moment approaches the flexible ring solution only at squatting levels outside the range usually encountered.

In addition to comparing the bending moments of the segmental ring to the analytical solution at the same ovalisation as discussed above, comparisons for the same ground stiffness can be made. The results are presented in Figure 17 in terms of the factor $m = \frac{M}{\sigma_v \cdot R^2}$ (where M is the bending moment) and the relative stiffness factor $\alpha = \frac{E_c \cdot R^3}{E \cdot I}$, (where *E* is the Young's modulus of the lining and *I* is the second moment of area of the segment cross-section), defined in Duddeck and Erdmann (1985). The relative stiffness $\alpha$ can be thought of as the factor governing the magnitude of the maximum lining bending moment. Since the ground stiffness provides a restriction to the deformation, as it reduces (and so does $\alpha$) the ring undergoes larger deformations and a greater stiffness degradation. This is illustrated in Figure 17 as, for reducing values of $\alpha$, the curve corresponding to the crown gradually diverges from the rigid ring solution and corresponds to lower *m* values from the point at which the 0° joint first opens ($\alpha \approx 55 m^{-1}$). At the axis level, on the other hand, the analytical solution is followed for almost the full range of $\alpha$ values under consideration, with a slightly higher factor *m* towards the low end of $\alpha$, which suggests that this cross-section is attracting an increasing amount of load due to the large stiffness reduction at the 0° joint. The above observations about Figure 17 can be summarised

as follows: for the same ground stiffness, in the segmental ring the bending moment at the crown tends to be lower (if the joint is open) than that of the rigid ring; at the axis level the bending moment tends to be of similar magnitude or higher than that of the rigid ring (for very low ground stiffness); and finally, the segmental ring undergoes larger squatting than the continuous ring (see Figure 16), reflecting the stiffness degradation occurring all around the ring. As such the difference in squatting can be employed as an overall measure of the ring stiffness reduction.

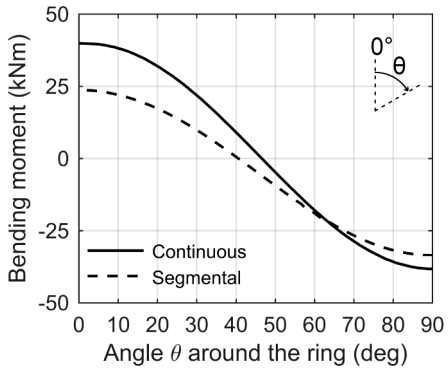


*Figure 15 Bending moment (kNm) distribution at approx. 1% squatting* (M+ tension intrados)

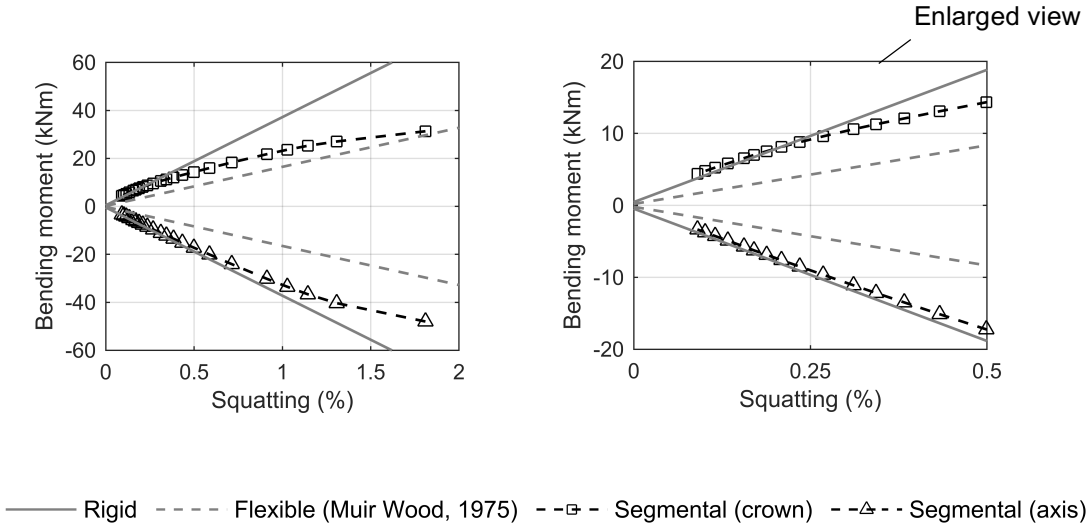


Figure 16 Bending moment (kNm) at crown/invert and axis level for a range of squatting magnitudes (% diameter) – segmental ring model vs elastic continuum

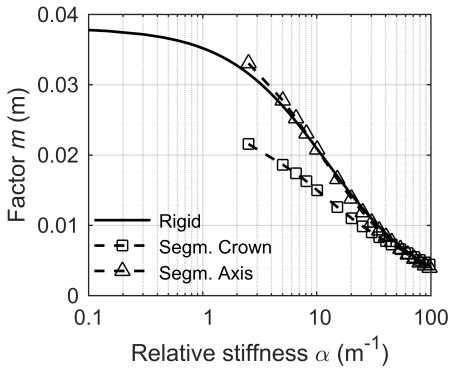


*Figure 17 Moment factor m against relative stiffness $\alpha$ – segmental ring model vs elastic continuum*

## 6.3 Discussion

The numerical results presented above indicate that the stiffness at the crown and the axis of the segmental GCI ring reduce nonlinearly with increasing ovalisation, which can be attributed to the gradual opening of the joints. Furthermore, it is shown that the degradation of the bending stiffness is significantly more pronounced around the crown than at the axis (these are the two sections where the maximum bending moments are expected under normal field conditions and therefore critical for engineering assessments). It should be noted that the stiffness degradation observed relates to the joint orientation considered in this study (joint aligned with the crown, middle segment aligned with axis level) and this needs to be taken into account when extrapolating to other GCI geometries where the joint orientations are different. Due to the inhomogeneous stiffness around the ring, the internal forces at the crown and the axis cannot be determined accurately by applying a unique bending stiffness to the elastic continuum model or to any other method that assumes that the lining is continuous. Thus, the use of the reduction formula proposed by Muir Wood (1975) may not be appropriate for GCI linings, as it predicts equal bending moments at the crown and the axis, and results in bending moments that are too low compared with those predicted numerically.

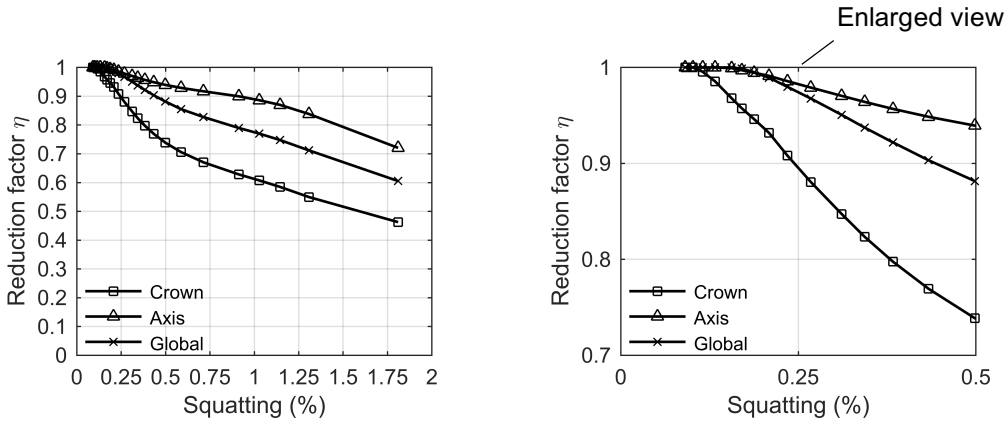


*Figure 18 Reduction factor $\eta$ for the crown, axis level sections and global response of the GCI ring*

An alternative approach is proposed here, with different reduction factors $\eta$ for the crown and axis, which allow the structural forces at those two locations to be determined from continuous ring solutions independently. The evolution of the reduction factor $\eta$ with squatting at the crown and the axis, as well as the factor $\eta$ of the global response are given in Figure 18. The crown and axis factors are obtained from the ratio of the bending moment in the segmental ring model to that in the rigid ring model for the same squatting magnitude:

$$\eta_c = \frac{M_c^s}{M_c^r} \tag{1}$$

$$\eta_a = \frac{M_a^s}{M_a^r} \tag{2}$$

where subscripts *c* and *a* denote crown and axis level respectively and superscripts *s* and *r* denote segmental and rigid respectively. Note that the rigid ring model was preferred over the analytical solution in order to obtain these factors, such that the small discrepancies between the two could be accounted for. The global reduction factor, $\eta_g$, on the other hand, is determined as the bending stiffness in the analytical solution required to match the squatting in the segmental model (for a given ground stiffness), divided by the bending stiffness of the segment cross-section (i.e. EI per m):

$$\eta_g = \frac{1}{12EI} \cdot \left( \frac{(\sigma_v - \sigma_h)R^4}{u_{2\varphi}^*} - \frac{(3-2v)E_c R^3}{(1+v)(3-4v)} \right) \tag{3}$$

where $u_{2\varphi}^*$ is the radial horizontal displacement obtained from the numerical model[1]. This factor constitutes a global measure of the ring stiffness reduction.

Generally, when assessing a tunnel in-situ condition, the only reliable field data relate to the horizontal ovalisation of the tunnel (in the absence of in-tunnel measurements of the tunnel in question, TfL (2017) recommends assuming 1% squatting), therefore, it seems reasonable to

[1] Note that in order to comply with the assumptions of the analytical solution where $u_{2\varphi}$ is the deviatoric component of the radial displacement (i.e. that attributed to the difference between the soil primary stresses), the value $u_{2\varphi}^*$ stands for the total radial displacement from the numerical model minus that attributed to the isotropic component of the soil primary stresses.

determine the tunnel internal forces according to the adopted ovalisation value. With this in mind, a simple methodology for the evaluation of the internal forces of GCI tunnels can be elaborated integrating the abovementioned reduction factors to account for the segmental nature of the tunnels. First, given the ovalisation of the tunnel, the bending moments at the critical sections (i.e. crown and axis level) are determined assuming a rigid ring (full bending stiffness). This is straightforward as analytical solutions predict the evolution of bending moments with tunnel ovalisation (see Figure 16). Second, the reduction factors $\eta_c$ and $\eta_a$ for the adopted tunnel squatting are obtained from the numerically-derived chart presented in Figure 18. The reduction factors can then be applied to correct the initial estimate of bending moments at both sections (see equations (1) and (2)). An analogous strategy can be applied to establish the change of internal forces in response to additional ground movements because in practice this calculation usually relies on soil displacements being obtained by some other method and subsequently applied to the solution given by Morgan (1961) to obtain the change in bending moments, the proposed factors can be adopted to correct the latter. Furthermore, the global factor can be employed to adjust the bending stiffness of the lining in geotechnical FE analyses where a continuous beam/shell approach is adopted to model the lining when the aim of the analysis is to assess the displacements of a GCI tunnel due to nearby construction/excavation works. Even though the conditions considered in this study are representative of a prototype LU running tunnel, additional studies should be performed in order to apply this methodology to a wider range of conditions, such as different tunnel depths, applying radial stresses only between the soil and the lining (i.e. full slip), and different joint configurations including the number (mainly relevant for station and crossover tunnels) and location of the joints. With respect to the latter, in cases where the rings are ‘rolled’, i.e. the longitudinal joints are not aligned along the tunnel axis, it would be necessary to consider a succession of several individual rings, with appropriately connected circumferential flanges.

## 7. Conclusions

This paper presents a number of FE analyses of a segmental GCI ring. In order to model failure of the GCI segments, a constitutive model, originally developed for shotcrete, was modified to be suitable for the modelling of GCI. The numerical model was carefully calibrated and validated with a series of laboratory tests conducted on a half-scale GCI ring at small and large distortions. The overall excellent ability of the numerical analysis to reproduce the experimentally observed behaviour in terms of the local behaviour of the longitudinal joints and of the stiffness reduction around the ring, inspires confidence in the predictive capabilities of the segmental ring model when subjected to field conditions.

Subsequently, a series of analyses replicating the assumptions of the elastic continuum method was conducted in order to evaluate the influence of the longitudinal joints on the structural response of a prototype GCI tunnel and to produce recommendations as how to account for the segmental nature of these tunnels in routine engineering calculations. Based on the differences established between the response of the segmental ring model and that of a continuous ring, a

set of reduction factors $\eta$ were produced for the range of squatting expected in the field. The factors derived for the crown and the axis can be adopted to 'correct' the bending moments estimated at those sections from analytical solutions, as well as to provide bounds to the bending stiffness of the lining at a given percentage of squatting. A global reduction factor was also provided as an average measure of the bending stiffness reduction which may be more appropriate for estimating distortions from ground movements in the GCI tunnel vicinity. These factors are strictly applicable only to the conditions (joints orientation, depth, etc.) encountered in a standard LU tunnel as adopted in this work, however, the developed methodology can be repeated under a wider range of conditions to produce generally applicable guidelines for assessing the influence of the longitudinal joints on the bending stiffness and internal forces of segmental GCI linings.

## 8. Acknowledgements

This research is funded by the Engineering and Physical Sciences Research Council (EPSRC) through a Doctoral Training Grant (Ref: EP/R512540/1) to the first author.

## 9. References

ABAQUS 2014. ABAQUS User's manual, Version 6.14. *Dassault Systémes Simulia Corp., Providence, RI.*

Afshan, S., Yu, J., Standing, J., Vollum, R. & Potts, D. 2017. Ultimate capacity of a segmental grey cast iron tunnel lining ring subjected to large deformations. *Tunnelling and Underground Space Technology,* 64**,** 74-84.

Altenbach, H., Stoychev, G. & Tushtev, K. 2001. On elastoplastic deformation of grey cast iron. *International journal of plasticity,* 17**,** 719-736.

Angus, H. T. 1976. *Cast iron: physical and engineering properties,* London, England, Butterworth and Co. Ltd.

Blom, C. 2002. *Design philosophy of segmented linings for tunnels in soft soils.* PhD Thesis, Delft University of Technology, the Netherlands.

Chen, A. C. & Chen, W.-F. 1975. Constitutive relations for concrete. *Journal of Engineering Mechanics,* 101**,** 465-481.

Coffin, L. F. 1950. The flow and fracture of a brittle material. *Journal of Applied Mechanics-Transactions Of The Asme,* 17**,** 233-248.

Craig, R. & Muir Wood, A., 1978. *A review of tunnel lining practice in the United Kingdom*. Document No. TRRL Suppl Rpt 335 Monograph

Day, R. & Potts, D. 1994. Zero thickness interface elements—numerical stability and application. *International Journal for numerical and analytical methods in geomechanics,* 18**,** 689-708.

Duddeck, H. & Erdmann, J. 1985. Structural design models for tunnels in soft soil. *Underground Space;(United States),* 9**,** 246-259.

Gilbert, G. Behaviour of cast irons under stress. B. C. I. R. A. Conf. on Engineering Properties of Performance of Modern Iron Castings, 1972, 41-73, 1972.

Hjelm, H. E. 1994. Yield surface for grey cast iron under biaxial stress. *Journal of Engineering Materials and Technology,* 116**,** 148-154.

Lee, K. & Ge, X. 2001. The equivalence of a jointed shield-driven tunnel lining to a continuous ring structure. *Canadian Geotechnical Journal,* 38**,** 461-483.

Li, Z., Soga, K., Wang, F., Wright, P. & Tsuno, K. 2014. Behaviour of cast-iron tunnel segmental joint from the 3D FE analyses and development of a new bolt-spring model. *Tunnelling and Underground Space Technology,* 41**,** 176-192.

Li, Z., Soga, K. & Wright, P. 2015. Behaviour of cast-iron bolted tunnels and their modelling. *Tunnelling and Underground Space Technology,* 50**,** 250-269.

Morgan, H. 1961. A contribution to the analysis of stress in a circular tunnel. *Géotechnique,* 11**,** 37-46.

Muir Wood, A. 1975. The circular tunnel in elastic ground. *Géotechnique,* 25**,** 115-127.

Plizzari, G. & Tiberti, G. 2006. Steel fibers as reinforcement for precast tunnel segments. *Tunnelling and Underground Space Technology,* 21**,** 438-439.

Potts, D. M. & Zdravkovic, L. 1999. *Finite element analysis in geotechnical engineering: theory,* London, Thomas Telford.

Puzrin, A. & Burland, J. B. 1996. A logarithmic stress–strain function for rocks and soils. *Géotechnique,* 46**,** 157-164.

Schutz, R. 2010. *Numerical modelling of shotcrete for tunnelling.* PhD Thesis, Imperial College London.

Standing, J., Potts, D., Vollum, R., Burland, J., Tsiampousi, A., Afshan, S., Yu, J., Wan, M. & Avgerinos, V. 2015. Investigating the effect of tunnelling on existing tunnels. Proc. Underground Design and Construction Tunnelling Conference, IOM3. Hong Kong.

Summersgill, F., Kontoe, S. & Potts, D. 2017. Critical assessment of nonlocal strain-softening methods in biaxial compression. *International Journal of Geomechanics,* 17**,** 04017006.

Teachavorasinskun, S. & Chub-uppakarn, T. 2010. Influence of segmental joints on tunnel lining. *Tunnelling and Underground Space Technology,* 25**,** 490-494.

TfL, 2017. Civil Engineering - Deep Tube Tunnels and Shafts. Standard S1055-A5

TfL, 2020. *Personal communication (email).*

Thomas, H. 1977. Measuring the structural performance of cast Iron tunnel linings in the laboratory. *Ground Engineering,* 10**,** 29-36.

Tsiampousi, A., Yu, J., Standing, J., Vollum, R. & Potts, D. 2017. Behaviour of bolted cast iron joints. *Tunnelling and Underground Space Technology,* 68**,** 113-129.

Tube Lines, 2008. *Cast iron Coring Report. Deep Tube Tunnel Knowledge and Inspection Programme Annual Work Plan 2. Revision 4 issued on 22/09/2008*. Document No. TLL-L001-N416-DTAAWP2-TUN-RPT-00019

Wright, P. J. 2013. Validation of soil parameters for deep tube tunnel assessment. *Proceedings of the Institution of Civil Engineers-Geotechnical Engineering,* 166**,** 18-30.

Ye, F., Gou, C.-f., Sun, H.-d., Liu, Y.-p., Xia, Y.-x. & Zhou, Z. 2014. Model test study on effective ratio of segment transverse bending rigidity of shield tunnel. *Tunnelling and Underground Space Technology,* 41**,** 193-205.

Young, W. C. & Budynas, R. G. 2002. *Roark's formulas for stress and strain*, McGraw-Hill New York.

Yu, J., Standing, J., Vollum, R., Potts, D. & Burland, J. 2017. Experimental investigations of bolted segmental grey cast iron lining behaviour. *Tunnelling and Underground Space Technology,* 61**,** 161-178.

Yu, J. B. Y. 2014. *Assessing ground interaction effects and potential damage on existing tunnels before and after new excavation works.* PhD Thesis, Imperial College London.

## Appendix A Constitutive modelling of GCI

A1 Model formulation

The main equations of the constitutive model implemented by Schutz (2010) and adapted by the authors for the modelling of GCI are presented below.

The tension yield surface $F_t$ is defined by a modified expression of the classical Rankine criterion:

$$F_t = p + \left[\left(\frac{2 \cdot J}{\sqrt{3}} \cdot sin\,(\theta + \frac{2\pi}{3})\right)^n + (a \cdot f_t)^n\right]^{\frac{1}{n}} - f_t \quad \text{(A1)}$$

where $p$ is the mean pressure, $J$ is the deviatoric stress, $\theta$ is the Lode angle and $f_t$ is the uniaxial tensile strength of the material. $a$ is the apex tolerance and determines the distance between the apex of the original and the modified Rankine surface along the hydrostatic axis, while $n$ controls the rounding of the surface. The compression yield surface $F_c$ follows that proposed by Chen and Chen (1975) which is defined by the following expression:

$$F_c = J^2 + \alpha_C \cdot f_c \cdot p - \beta_c \cdot f_c^2 \quad \text{(A2)}$$

where $f_c$ is the uniaxial compressive strength and parameters $\alpha_C$ and $\beta_c$ are defined as follows:

$$\alpha_c = \frac{e^2 - 1}{2 \cdot e - 1} \quad \text{(A3)}$$

$$\beta_c = \frac{2 \cdot e - e^2}{3(2 \cdot e - 1)} \quad \text{(A4)}$$

$e$ is a dimensionless biaxial strength parameter. Note that if $e$ is set to 1, the yield surface expression reduces to the von Mises criterion. Note that associated conditions are assumed such that the plastic potentials for tension and compression adopt expressions A1 and A2, respectively. Regarding the hardening behaviour of the model, the evolution of the yield surfaces depends on the uniaxial stress-strain behaviour in tension and compression such that $f_t$ and $f_c$ evolve with respect to the major and minor principal plastic strains, $\varepsilon_1^p$ and $\varepsilon_3^p$, respectively. The hardening curve of both surfaces consist of several sections, as shown schematically in Figure A1: strain-hardening from yield to peak strength and strain-softening

from peak to residual strength (linear and exponential softening available for tension) followed by constant residual strength.

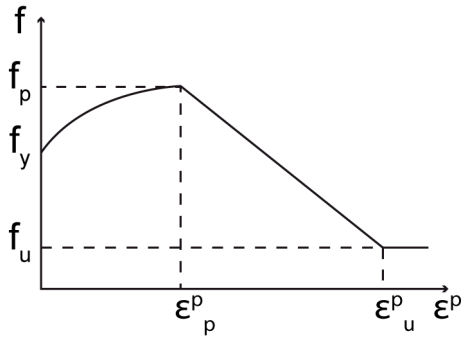


*Figure A1 Sketch of model hardening curve*

The pre-peak hardening expression originally implemented in the model was found inadequate for the modelling of GCI and it was replaced, for tension and compression, by the expression introduced by Puzrin and Burland (1996), which was meant to reproduce the pre-yield nonlinear behaviour of soils but is also suitable for the modelling of GCI as shown in this work. The formula of the new hardening law is presented below:

$$f = f_y + K_i \cdot \varepsilon^p \cdot \left[1 - \alpha \cdot \left(\ln\left(1 + \frac{K_i \cdot \varepsilon^p}{f_p - f_y}\right)\right)^{R_L}\right] \tag{A5}$$

where $\varepsilon^p$ is the plastic strain (hardening variable), $f$ is the uniaxial strength, $f_y$ is the uniaxial yield strength, $f_p$ is the uniaxial peak strength, $K_i$ is the initial tangent stiffness of the hardening curve. $\alpha$ and $R_L$ are constants defined by the expressions:

$$R_L = \frac{c \cdot (1 + x_L) \cdot \ln(1 + x_L)}{x_L \cdot (x_L - 1)} \tag{A6}$$

$$\alpha = \frac{(x_L - 1)}{x_L \cdot [\ln(1 + x_L)]^{R_L}} \tag{A7}$$

where *c* is a fitting parameter and $x_L$ is determined from:

$$x_L = \frac{K_i \cdot \varepsilon_p^p}{f_p - f_y} \tag{A8}$$

where $\varepsilon_p^p$ is the plastic strain at peak strength. The new hardening law therefore requires five parameters: the uniaxial yield stress $f_y$, the uniaxial peak strength $f_p$, the plastic strain at peak strength $\varepsilon_p^p$ and the fitting parameters $K_i$ and $c$.

Due to the presence of graphite flakes embedded in the steel matrix, GCI exhibits brittle behaviour in tension as it fractures at low levels of plastic strain (see Figure 4), this behaviour can be modelled within a continuum framework by strain-softening. However, it is well known that adopting standard strain-softening models leads to finite element solutions that are pathologically dependent on the spatial discretization when strain localization occurs. In order to overcome this limitation, the constitutive model needs to be complemented with a regularization technique that, in some way or another, incorporates a characteristic length into the formulation. In order to model fracturing of GCI, the model by Schutz (2010) has been extended with two different regularization methods: the fracture energy approach (i.e. mesh-dependent softening modulus) and the nonlocal method (Summersgill et al., 2017).

A2 Validation of the model

The constitutive model above was validated through comparison with the element tests conducted by Coffin (1950). Four single element simulations were performed aiming to validate the model under tensile yielding: uniaxial tensile test, biaxial tensile test with equal stresses $\sigma_1=\sigma_2$, biaxial tensile test with non-equal stresses $\sigma_1=2\sigma_2$, and pure shear test. The elastic modulus was 100 GPa, the Poisson's ratio was 0.227, the tensile yield stress was 56 MPa, the tensile peak strength was 225 MPa and the plastic strain $\varepsilon_1^p$ at peak strength was 0.25%. Figure A2 shows an overall good agreement between the numerical results and the laboratory data, with the exception of the pure shear test where the strains predicted by the model underestimate the laboratory measurements. The performance of the constitutive model is considered satisfactory for its use in boundary value problems.

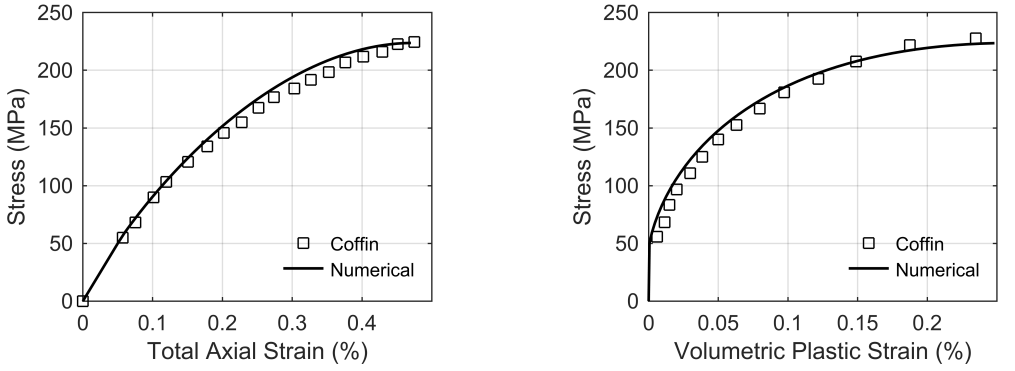


Uniaxial tensile test

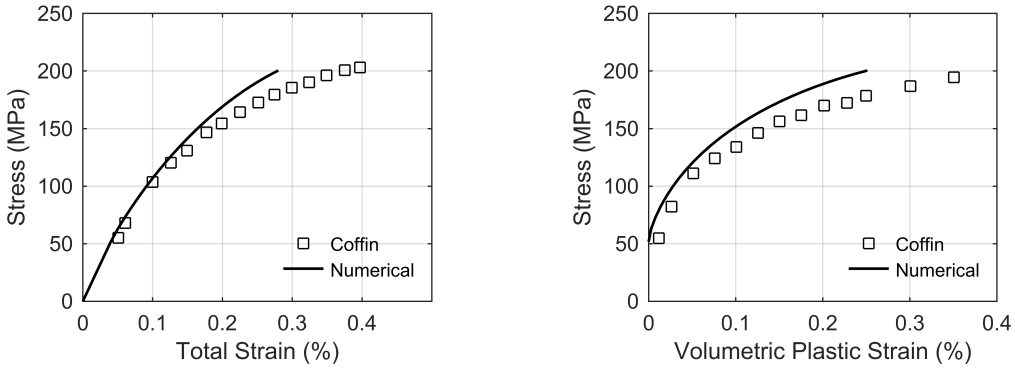


Equal $\sigma_1=\sigma_2$ biaxial test

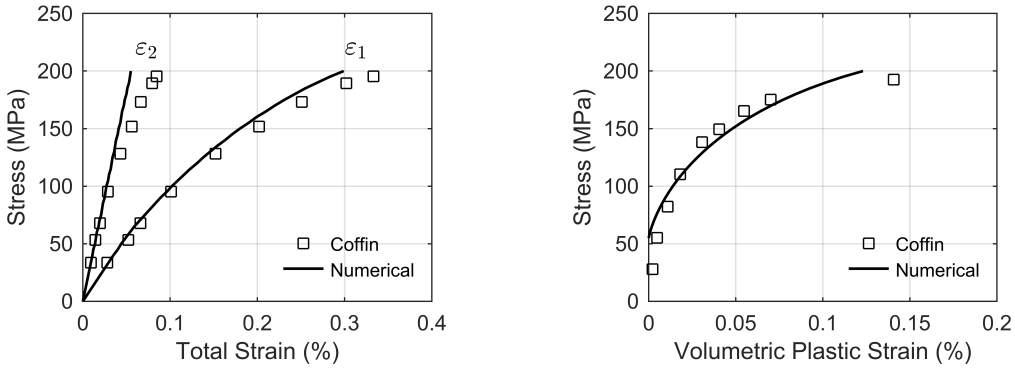


Non-equal $\sigma_1=2\sigma_2$ biaxial test

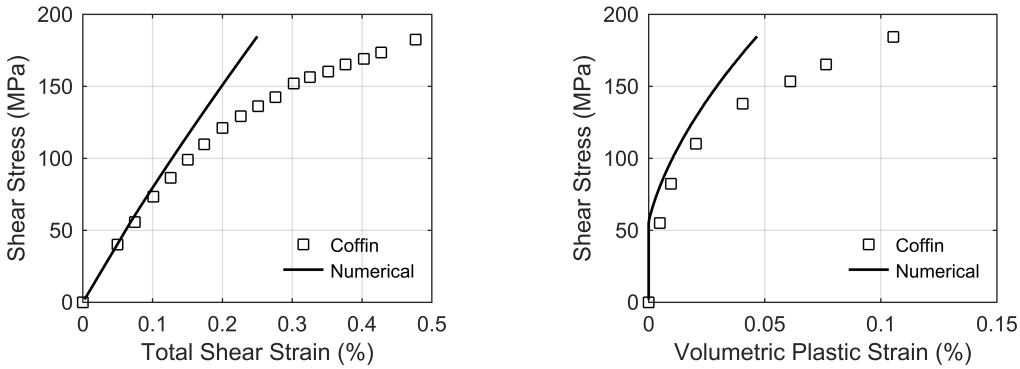


Pure shear test

*Figure A2 Series of single element simulations under different loading paths, comparison between numerical predictions and experimental data (Coffin, 1950)*

A3 Parameters adopted for GCI segments

| Model parameters | Value |
|---|---|
| Tensile yield stress $f_{ty}$ | 40 MPa |
| Tensile peak strength $f_{tp}$ | 140 MPa |
| Plastic tensile strain at peak $\varepsilon_{tp}^{p}$ | 0.55% |
| Compressive yield stress $f_{cy}$ | 160 MPa |
| Compressive peak strength $f_{cp}$ | 560 MPa |
| Plastic compressive strain at peak $\varepsilon_{cp}^{p}$ | 0.55 % |
| Biaxial strength parameter *e* | 1.0 (von Mises) |
| Hardening parameter tension $K_{i,t}$ | $10^6$ MPa |
| Hardening parameter tension $c_t$ | 1.0 |
| Hardening parameter compression $K_{i,c}$ | $10^6$ MPa |
| Hardening parameter compression $c_c$ | 1.0 |

*Table A1 Plastic parameters for the modelling of GCI segments*

## Appendix B Analyses at small distortions with loading perturbations

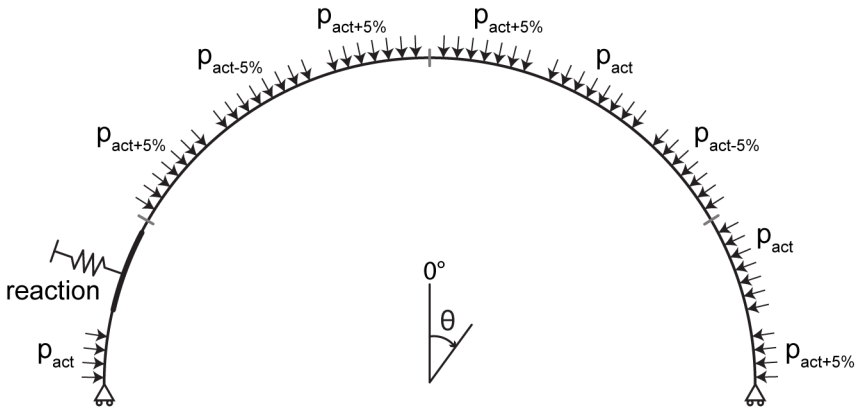


*Figure B1 Sketch of the loading configuration*

Imperfections in stress transfer across the joint in the experiment, which are not included in the numerical model, where joint plates were perfectly flat and segments perfectly aligned in the experiment, may explain the slight disagreement with laboratory data at small distortions. To demonstrate this, a set of analyses including a degree of perturbation in the model conditions was conducted, where the confinement load was varied at a number of actuators by 5% above/below their prescribed value (Figure B1). The bending moment change (Figure B2) and the joint opening (Figure B3) are very well captured for all confinement loads.

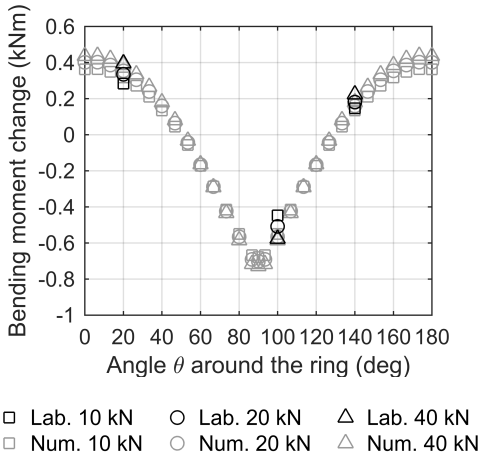


*Figure B2 Bending moment change (kNm) distribution for different confinements with loading perturbation (M+ tension intrados)*

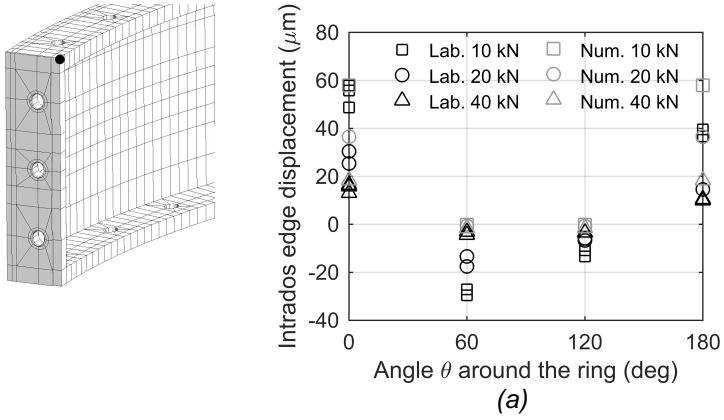


*(a)*

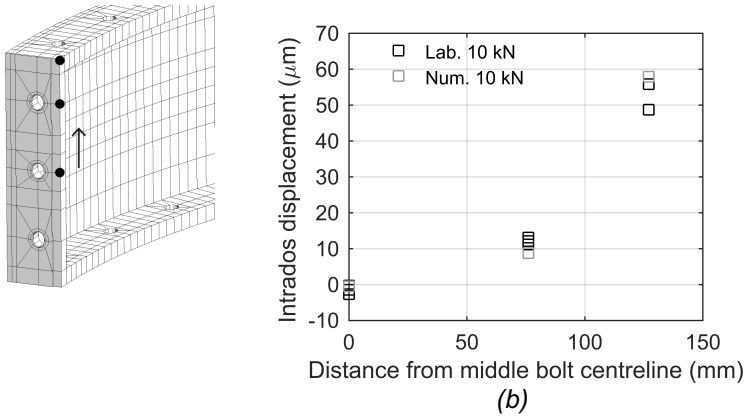


*(b)*

*Figure B3* Displacement (μm) at the intrados with loading perturbation (a) at the upper edge location of joints around the ring for all confinement cases (b) along the intrados of the 0º joint in the 10 kN load case (opening is positive)